Space Telescope and Optical Reverberation Mapping project: IX. Velocity-delay maps for broad emission lines in NGC 5548

Horne, K.; De Rosa, G.; Peterson, B.M.; Barth, A.J.; Ely, J.; Fausnaugh, M.M.; ... ; Zu, Y.

Citation

Horne, K., De Rosa, G., Peterson, B. M., Barth, A. J., Ely, J., Fausnaugh, M. M., ... Zu, Y. (2021). Space Telescope and Optical Reverberation Mapping project: IX. Velocity-delay maps for broad emission lines in NGC 5548. *The Astrophysical Journal*, *907*(2). doi:10.3847/1538-4357/abce60

Draft version November 21, 2021
Typeset using LaTeX **twocolumn** style in AASTeX62

Space Telescope and Optical Reverberation Mapping Project.
IX. Velocity-Delay Maps for Broad Emission Lines in NGC 5548

Keith Horne,[1] G. De Rosa,[2] B. M. Peterson,[2,3,4] A. J. Barth,[5] J. Ely,[2] M. M. Fausnaugh,[3,6] G. A. Kriss,[2] L. Pei,[5]
S. M. Adams,[3,7] M. D. Anderson,[8] P. Arévalo,[9] T G. Beatty,[3,10,11] V. N. Bennert,[12] M. C. Bentz,[8] A. Bigley,[13]
S. Bisogni,[3,14,15] G. A. Borman,[16] T. A. Boroson,[17] M. C. Bottorff,[18] W. N. Brandt,[10,19,20] A. A. Breeveld,[21]
M. Brotherton,[22] J. E. Brown,[23] J. S. Brown,[3] E. M. Cackett,[24] G. Canalizo,[25] M. T. Carini,[26] K. I. Clubb,[13]
J. M. Comerford,[27] E. M. Corsini,[28,29] D. M. Crenshaw,[8] S. Croft,[13] K. V. Croxall,[3,4,30] E. Dalla Bontà,[28,29]
A. J. Deason,[31,32] M. Dehghanian,[33] A. De Lorenzo-Cáceres,[1,34] K. D. Denney,[3,4,30] M. Dietrich,[35,*] C. Done,[36]
R. Edelson,[37] N. V. Efimova,[38] M. Eracleous,[10,20] P. A. Evans,[39] G. J. Ferland,[33] A. V. Filippenko,[13,40] K. Flatland,[41,42]
O. D. Fox,[13,2] E. Gardner,[36,43] E. L. Gates,[44] N. Gehrels,[45,†] S. Geier,[46,47,48] J. M. Gelbord,[49,50] M. R. Goad,[39]
L. Gonzalez,[41] V. Gorjian,[51] J. E. Greene,[52] C. J. Grier,[3,10,20,53] D. Grupe,[54] A. Gupta,[3] P. B. Hall,[55]
C. B. Henderson,[3,51,‡] S. Hicks,[26] E. Holmbeck,[56] T. W.-S. Holoien,[3,4,57] T. Hutchison,[18,58,59] M. Im,[60] J. J. Jensen,[61]
C. A. Johnson,[62] M. D. Joner,[63] J. Jones,[8] J. Kaastra,[64,65] S. Kaspi,[66,67] P. L. Kelly,[13,68] J. A. Kennea,[10] M. Kim,[69,70]
S. Kim,[3,4] S. C. Kim,[69] A. King,[71] S. A. Klimanov,[38] C. S. Kochanek,[3,4] K. T. Korista,[72] Y. Krongold,[73] M. W. Lau,[25]
J. C. Lee,[69] D. C. Leonard,[41] Miao Li,[74] P. Lira,[75] C. Lochhaas,[3] Zhiyuan Ma,[23] F. MacInnis,[18] M. A. Malkan,[56]
E. R. Manne-Nicholas,[8] S. Mathur,[3,4] J. C. Mauerhan,[13] R. McGurk,[31,57] I. M. McHardy,[76] C. Montuori,[77]
L. Morelli,[28,29,78] A. Mosquera,[3,79] D. Mudd,[3,5] F. Müller–Sánchez,[27] S. V. Nazarov,[16] H. Netzer,[66] R. P. Norris,[8]
J. A. Nousek,[10] M. L. Nguyen,[22] P. Ochner,[28,29] D. N. Okhmat,[16] A. Pancoast,[15,§] I. Papadakis,[80,81] J. R. Parks,[8]
M. T. Penny,[3] A. Pizzella,[28,29] R. W. Pogge,[3,4] R. Poleski,[3] J.-U. Pott,[82] D. Proga,[83] S. E. Rafter,[67,84] H.-W. Rix,[82]
J. Runnoe,[85] D. A. Saylor,[8] J. S. Schimoia,[3,86] K. Schnülle,[82] B. Scott,[25] S. G. Sergeev,[16] B. J. Shappee,[3,87]
I. Shivvers,[13] M. Siegel,[17] G. V. Simonian,[3] A. Siviero,[28] A. Skielboe,[61] G. Somers,[3,88] M. Spencer,[63] D. Starkey,[1,89]
D. J. Stevens,[3,10,11] M. A. Strauss,[52] H.-I. Sung,[69] J. Tayar,[3,87,¶] K. G. Teems,[8] N. Tejos,[90] T. Treu,[56,**] C. S. Turner,[8]
P. Uttley,[91] J . Van Saders,[3,87] M. Vestergaard,[61,53] L. Vican,[56] S. Villanueva Jr.,[3] C. Villforth,[92] Y. Weiss,[67]
J.-H. Woo,[60] H. Yan,[23] S. Young,[37] H. Yuk,[13] N. L. Zakamska,[93] W. Zheng,[13] W. Zhu,[3] and Y. Zu[3,94]

[1] *SUPA Physics and Astronomy, University of St. Andrews, Fife, KY16 9SS Scotland, UK*

[2] *Space Telescope Science Institute, 3700 San Martin Drive, Baltimore, MD 21218, USA*

[3] *Department of Astronomy, The Ohio State University, 140 W 18th Ave, Columbus, OH 43210, USA*

[4] *Center for Cosmology and AstroParticle Physics, The Ohio State University, 191 West Woodruff Ave, Columbus, OH 43210, USA*

[5] *Department of Physics and Astronomy, 4129 Frederick Reines Hall, University of California, Irvine, CA 92697, USA*

[6] *Kavli Institute for Space and Astrophysics Research, Massachusetts Institute of Technology, 77 Massachusetts Avenue, Cambridge, MA 02139-4307, USA*

[7] *Cahill Center for Astrophysics, California Institute of Technology, Pasadena, CA 91125, USA*

[8] *Department of Physics and Astronomy, Georgia State University, 25 Park Place, Suite 605, Atlanta, GA 30303, USA*

[9] *Instituto de Física y Astronomía, Facultad de Ciencias, Universidad de Valparaíso, Gran Bretana N 1111, Playa Ancha, Valparaíso, Chile*

[10] *Department of Astronomy and Astrophysics, Eberly College of Science, The Pennsylvania State University, 525 Davey Laboratory, University Park, PA 16802, USA*

[11] *Center for Exoplanets and Habitable Worlds, The Pennsylvania State University, University Park, PA 16802, USA*

[12] *Physics Department, California Polytechnic State University, San Luis Obispo, CA 93407, USA*

[13] *Department of Astronomy, University of California, Berkeley, CA 94720-3411, USA*

[14] *Osservatorio Astrofisico di Arcetri, largo E. Fermi 5, 50125, Firenze, Italy*

[15] *Harvard-Smithsonian Center for Astrophysics, 60 Garden Street, Cambridge, MA 02138, USA*

[16] *Crimean Astrophysical Observatory, P/O Nauchny, Crimea 298409*

[17] *Las Cumbres Observatory Global Telescope Network, 6740 Cortona Drive, Suite 102, Goleta, CA 93117, USA*

[18] *Fountainwood Observatory, Department of Physics FJS 149, Southwestern University, 1011 E. University Ave., Georgetown, TX 78626, USA*

[19] *Department of Physics, The Pennsylvania State University, 104 Davey Laboratory, University Park, PA 16802, USA*

[20] *Institute for Gravitation and the Cosmos, The Pennsylvania State University, University Park, PA 16802, USA*

[21] *Mullard Space Science Laboratory, University College London, Holmbury St. Mary, Dorking, Surrey RH5 6NT, UK*

[22] *Department of Physics and Astronomy, University of Wyoming, 1000 E. University Ave. Laramie, WY 82071, USA*

[23] *Department of Physics and Astronomy, University of Missouri, Columbia, MO 65211, USA*

[24] *Department of Physics and Astronomy, Wayne State University, 666 W. Hancock St, Detroit, MI 48201, USA*

[25] *Department of Physics and Astronomy, University of California, Riverside, CA 92521, USA*

[26] *Department of Physics and Astronomy, Western Kentucky University, 1906 College Heights Blvd #11077, Bowling Green, KY 42101, USA*

[27] *Department of Astrophysical and Planetary Sciences, University of Colorado, Boulder, CO 80309, USA*

[28] *Dipartimento di Fisica e Astronomia "G. Galilei," Università di Padova, Vicolo dell'Osservatorio 3, I-35122 Padova, Italy*

[29] *INAF-Osservatorio Astronomico di Padova, Vicolo dell'Osservatorio 5 I-35122, Padova, Italy*

[30]Illumination Works, LLC, 5650 Blazer Parkway, Dublin, OH 43017, USA
[31]Department of Astronomy and Astrophysics, University of California Santa Cruz, 1156 High Street, Santa Cruz, CA 95064, USA
[32]Institute for Computational Cosmology, Department of Physics, University of Durham, South Road, Durham DH1 3LE, UK
[33]Department of Physics and Astronomy, The University of Kentucky, Lexington, KY 40506, USA
[34]Instituto de Astrofísica de Canarias, Calle Vía Láctea s/n, E-38205 La Laguna, Tenerife, Spain
[35]Department of Earth, Environment and Physics, Worcester State University, Worcester, MA 01602, USA
[36]Centre for Extragalactic Astronomy, Department of Physics, University of Durham, South Road, Durham DH1 3LE, UK
[37]Department of Astronomy, University of Maryland, College Park, MD 20742, USA
[38]Pulkovo Observatory, 196140 St. Petersburg, Russia
[39]Department of Physics and Astronomy, University of Leicester, University Road, Leicester, LE1 7RH, UK
[40]Miller Senior Fellow, Miller Institute for Basic Research in Science, University of California, Berkeley, CA 94720, USA
[41]Department of Astronomy, San Diego State University, San Diego, CA 92182, USA
[42]Oakwood School, 105 John Wilson Way, Morgan Hill, CA 95037, USA
[43]School of Biological Sciences, University of Reading, Whiteknights, Reading, RG6 6AS, UK
[44]Lick Observatory, P.O. Box 85, Mt. Hamilton, CA 95140, USA
[45]Astrophysics Science Division, NASA Goddard Space Flight Center, Mail Code 661, Greenbelt, MD 20771, USA
[46]Instituto de Astrofísica de Canarias, 38200 La Laguna, Tenerife, Spain
[47]Departamento de Astrofísica, Universidad de La Laguna, E-38206 La Laguna, Tenerife, Spain
[48]Gran Telescopio Canarias (GRANTECAN), 38205 San Cristóbal de La Laguna, Tenerife, Spain
[49]Spectral Sciences Inc., 4 Fourth Ave., Burlington, MA 01803, USA
[50]Eureka Scientific Inc., 2452 Delmer St. Suite 100, Oakland, CA 94602, USA
[51]Jet Propulsion Laboratory, California Institute of Technology, 4800 Oak Grove Drive, Pasadena, CA 91109, USA
[52]Department of Astrophysical Sciences, Princeton University, Princeton, NJ 08544, USA
[53]Steward Observatory, University of Arizona, 933 North Cherry Avenue, Tucson, AZ 85721, USA
[54]Space Science Center, Morehead State University, 235 Martindale Dr., Morehead, KY 40351, USA
[55]Department of Physics and Astronomy, York University, Toronto, ON M3J 1P3, Canada
[56]Department of Physics and Astronomy, University of California, Los Angeles, CA 90095, USA
[57]Carnegie Observatories, 813 Santa Barbara Street, Pasadena, CA 91101, USA
[58]Department of Physics and Astronomy, Texas A&M University, College Station, TX, 77843-4242 USA
[59]George P. and Cynthia Woods Mitchell Institute for Fundamental Physics and Astronomy,
Texas A&M University, College Station, TX, 77843-4242 USA
[60]Astronomy Program, Department of Physics & Astronomy, Seoul National University, Seoul, Republic of Korea
[61]Dark Cosmology Centre, Niels Bohr Institute, University of Copenhagen, Juliane Maries Vej 30, DK-2100 Copenhagen Ø, Denmark
[62]Santa Cruz Institute for Particle Physics and Department of Physics, University of California, Santa Cruz, CA 95064, USA
[63]Department of Physics and Astronomy, N283 ESC, Brigham Young University, Provo, UT 84602, USA
[64]SRON Netherlands Institute for Space Research, Sorbonnelaan 2, 3584 CA Utrecht, The Netherlands
[65]Leiden Observatory, Leiden University, PO Box 9513, 2300 RA Leiden, The Netherlands
[66]School of Physics and Astronomy, Raymond and Beverly Sackler Faculty of Exact Sciences, Tel Aviv University, Tel Aviv 69978, Israel
[67]Physics Department, Technion, Haifa 32000, Israel
[68]Minnesota Institute for Astrophysics, School of Physics and Astronomy, 116 Church Street S.E., University of Minnesota, Minneapolis, MN 55455, USA
[69]Korea Astronomy and Space Science Institute, Republic of Korea
[70]Department of Astronomy and Atmospheric Sciences, Kyungpook National University, Daegu 41566, Korea
[71]School of Physics, University of Melbourne, Parkville, VIC 3010, Australia.
[72]Department of Physics, Western Michigan University, 1120 Everett Tower, Kalamazoo, MI 49008, USA
[73]Instituto de Astronomía, Universidad Nacional Autonoma de Mexico, Cuidad de Mexico, Mexico
[74]Department of Astronomy, Columbia University, 550 W120th Street, New York, NY 10027, USA
[75]Departamento de Astronomia, Universidad de Chile, Camino del Observatorio 1515, Santiago, Chile
[76]University of Southampton, Highfield, Southampton, SO17 1BJ, UK
[77]DiSAT, Universita dell'Insubria, via Valleggio 11, 22100, Como, Italy
[78]Instituto de Astronomia y Ciencias Planetarias, Universidad de Atacama, Copiapó, Chile
[79]Physics Department, United States Naval Academy, Annapolis, MD 21403, USA
[80]Department of Physics and Institute of Theoretical and Computational Physics, University of Crete, GR-71003 Heraklion, Greece
[81]IESL, Foundation for Research and Technology, GR-71110 Heraklion, Greece
[82]Max Planck Institut für Astronomie, Königstuhl 17, D–69117 Heidelberg, Germany
[83]Department of Physics & Astronomy, University of Nevada, Las Vegas, 4505 South Maryland Parkway, Box 454002, Las Vegas, NV 89154-4002, USA
[84]Department of Physics, Faculty of Natural Sciences, University of Haifa, Haifa 31905, Israel
[85]Department of Astronomy, University of Michigan, 1085 S. University Avenue, Ann Arbor, MI 48109, USA

[86]*Laboratório Interinstitucional de e-Astronomia, Rua General José Cristino, 77 Vasco da Gama, Rio de Janeiro, RJ – Brazil*
[87]*Institute for Astronomy, 2680 Woodlawn Drive, Honolulu, HI 96822-1839, USA*
[88]*Department of Physics and Astronomy, Vanderbilt University, 6301 Stevenson Circle, Nashville, TN 37235, USA*
[89]*Department of Astronomy, University of Illinois Urbana-Champaign, 1002 W. Green Street, Urbana, IL 61801, USA*
[90]*Instituto de Física, Pontificia Universidad Católica de Valparaíso, Casilla 4059, Valparaíso, Chile*
[91]*Astronomical Institute 'Anton Pannekoek,' University of Amsterdam, Postbus 94249, NL-1090 GE Amsterdam, The Netherlands*
[92]*University of Bath, Department of Physics, Claverton Down, BA2 7AY, Bath, UK*
[93]*Department of Physics and Astronomy, The Johns Hopkins University, Baltimore, MD 21218, USA*
[94]*Shanghai Jiao Tong University, 800 Dongchuan Road, Shanghai, 200240, China*

ABSTRACT

In this contribution, we achieve the primary goal of the AGN STORM campaign by recovering velocity-delay maps, which are the key to understanding the geometry, ionization structure, and kinematics of the broad-line region, for the prominent broad emission lines, Lyα, C IV, He II and Hβ, in the spectrum of NGC 5548. The emission-line responses inhabit the interior of a virial envelope. The velocity-delay maps reveal stratified ionization structure. The He II response inside 5–10 light days has a broad single-peaked velocity profile. The Lyα, C IV, and Hβ responses peak inside 10 light days, extend outside 20 light days, and exhibit a velocity profile with two peaks separated by 5000 km s^{-1} in the 10–20 light-day delay range. The velocity-delay maps show that the "M"-shaped lag vs. velocity structure found in previous cross-correlation analysis is the signature of a Keplerian disk with a well-defined outer edge at $R/c = 20$ light days. The outer wings of the "M" arise from the virial envelope, and the "U"-shaped interior of the "M" is the lower half of an ellipse in the velocity–delay plane. The far side response is weaker than that from the near side, so that we see clearly the lower half, but only faintly the upper half, of the velocity–delay ellipse. The delay $\tau = (R/c)(1-\sin i) = 5$ light days at line center is from the near edge of the inclined ring, giving the inclination $i = 45°$. A black hole mass of $M_{\rm BH} = 7\times10^7\ M_\odot$ is consistent with the velocity-delay structure. A 'barber pole' pattern with stripes moving from red to blue across the C IV and possibly Lyα line profiles suggests the presence of azimuthal structure rotating around the far side of the broad-line region and may be the signature of precession or orbital motion of structures in the inner disk. Further *HST* observations of NGC 5548 over a multi-year timespan but with a cadence of perhaps 10 days rather than 1 day could help to clarify the nature of this new AGN phenomenon.

Keywords: galaxies:active – galaxies:individual (NGC 5548) – galaxies:nuclei –galaxies:Seyfert

1. INTRODUCTION

Active galactic nuclei (AGN) are understood to be powered by accretion onto supermassive black holes in the nuclei of their host galaxies. On account of angular momentum and viscosity, accreted gas forms a disk on scales of a few to a few hundred gravitational radii, $R_{\rm g} = GM_{\rm BH}/c^2$, where $M_{\rm BH}$ is the mass of the central black hole. The accretion disk ionizes gas on scales of hundreds to thousands $R_{\rm g}$, which reprocesses the ionizing radiation into strong emission lines that are significantly Doppler-broadened by their motion in the deep gravitational potential of the black hole. However, the structure and kinematics of the "broad-line region" (BLR) remain one of the long-standing unsolved problems in AGN astrophysics.

It is generally supposed that the BLR plays some role in both inflow and outflow processes that are known to occur on these spatial scales. There is evidence for disk structure in some cases (e.g., Wills & Browne 1986; Eracleous & Halpern 1994; Vestergaard, Wilkes, & Barthel 2000; Eracleous & Halpern 2003; Strateva, et al. 2003; Smith, et al. 2004; Jarvis & McLure 2006; Gezari, et al. 2007; Young, et al. 2007; Lewis, Eracleous, & Storchi-Bergmann 2010; Storchi-Bergmann, et al. 2017) as well as evidence that gravity dominates the dynamics of the BLR (e.g., Peterson et al. 2004), although radiation pressure may also contribute (Marconi, et al. 2008; Netzer & Marziani 2010).

The reverberation mapping (RM) technique (Blandford & McKee 1982; Peterson 1993, 2014) affords a means of highly constraining the BLR geometry and kinematics by measurement of the time-delayed response to changes in the continuum flux as a function of Doppler velocity. The projection of the BLR velocity field and structure into the observables of Doppler velocity and time delay yields a "velocity–delay map." Velocity–delay maps provide detailed information on the BLR geometry, velocity field, and ionization structure, and can be constructed by analyzing the reverberating velocity profiles (Horne, et al. 2004). This requires sustained monitoring of the reverberating spectrum with high signal-to-noise ratio and high cadence to record the subtle changes in line profile.

---

[*] Deceased, 19 July 2018
[†] Deceased, 6 February 2017
[‡] NASA Postdoctoral Program Fellow
[§] Einstein Fellow
[¶] Hubble Fellow
[**] Packard Fellow

1.1. *The 2014 STORM Campaign on NGC 5548.*

Primarily in order to secure data suitable for velocity–delay mapping, NGC 5548 was the focus of intensive monitoring during a 2014 monitoring campaign, the AGN Space Telescope and Optical Reverberation Mapping (AGN STORM) program. Ultraviolet (UV) spectra were obtained almost daily for 6 months with the Cosmic Origins Spectrograph on *Hubble Space Telescope* (*HST*), securing 171 UV spectra covering rest-frame wavelengths 1120–1750 Å, including the prominent Lyα λ1216 and C IV λ1549 emission lines and weaker Si IV λ1397 and He II λ1640 emission lines (De Rosa, et al. 2015, hereafter Paper I). During the middle two-thirds of the campaign, observations with *Swift* provided longer-wavelength UV, 0.3 to 10 keV X-ray, and optical (*UBV*) continuum measurements (Edelson, et al. 2015, hereafter Paper II). A major ground-based campaign secured imaging photometry (Fausnaugh, et al. 2016, hereafter Paper III) with sub-diurnal cadence, including *UBV* and Sloan *ugriz* bandpasses. Optical spectroscopic observations (Pei, et al. 2017, hereafter Paper V) were also obtained, covering the Balmer line Hβ λ4861 and He II λ4686.

Anomalous behaviour in the emission-line response, known colloquially as the 'BLR holiday', is discussed by (Goad, et al. 2016, hereafter Paper IV). Detailed fitting of a reverberating disk model to the HST, *Swift*, and optical lightcurves was accomplished in (Starkey, et al. 2016, hereafter Paper VI). The X-ray observations are discussed in (Mathur, et al. 2017, hereafter Paper VII) and analysis of absorption line analysis in (Kriss, et al. 2018, hereafter Paper VIII). This paper, presenting velocity-delay maps derived from the spectral variations, is Paper IX of the STORM series.

Analysis of the superb and unprecedented STORM datasets has provided several surprises that challenge our previous understanding of AGN accretion flows:

- From the continuum and broad-band photometric light curves, cross-correlation analysis (Papers II and III) and detailed light curve modeling (Paper VI) show that the time-delay spectrum is flatter than expected, $\tau \propto \lambda^1$ rather than $\tau \propto \lambda^{4/3}$. This implies a steeper temperature profile for the accretion disk, $T \propto r^{-1}$ rather than $r^{-3/4}$.

- The observed spectrum is much fainter than predicted using the $T(r)$ law from $\tau(\lambda)$ (Paper VI). The disk surface seems to have a much higher color temperature, $T(r)$ from the time-delay spectrum $\tau(\lambda)$, than its brightness temperature, $T(r)$ from the flux spectrum $F_\nu(\lambda)$. This is a major challenge to accretion disk theory with implications that are not yet understood. One possibility is large-grained gray dust obscuring the AGN. Another is strong local temperature structures, or azimuthal structure casting shadows on the irradiated disk surface.

- The inferred lightcurve needed to drive reverberations in the UV and optical differs in detail from the X-ray lightcurve (Paper VI), being smoother and lacking the rapid variations seen in the X-rays. Gardner & Done (2017) have suggested that the observations imply that the standard disk is largely replaced by a geometrically thick Comptonized region.

- A significant anomaly in the broad emission line behavior, the 'BLR holiday', was identified and interpreted (Paper IV). The emission lines track continuum variations as expected in the first 1/3 of the STORM campaign, but then become fainter than expected in the latter 2/3, recovering just before the end. This anomalous period violates the expected behavior of emission lines reverberating with time delays relative to the continuum. Significant changes in line ratios occur, suggesting partial covering of a structured BLR, and/or changes in the shape of the ionizing spectrum. The likely interpretation is that part of the BLR is temporarily obscured to our line of sight and/or shielded from the ionizing radiation.

- Significant broad and narrow absorption lines are seen in the UV spectra (Paper VIII). Narrow absorption lines exhibit equivalent width variations that correlate with the continuum variations. Here the time delays reflect recombination times, there being no light travel-time delays since absorption occurs along the line of sight. The inferred density of $\sim 10^5$ cm^{-3} and location at 3 pc is compatible with clouds in the NLR (Peterson et al. 2013).

The focus of this paper is an echo-mapping analysis of the emission-line variations recorded in the STORM data. Section 2 briefly describes the *HST* and MDM Observatory spectra and the PREPSPEC analysis used to adjust calibrations, extract mean and rms spectra, continuum and emission-line light curves, and evidence for line profile changes. Section 2.4 discusses residuals to the PREPSPEC fit, including a "barber pole" pattern suggestive of a rotating structure. Section 3 discusses the linearized echo model and MEMECHO fit to the emission-line light curves as time-delayed echos of the 1158 Å continuum light curve, recovering the one-dimensional delay maps $\Psi(\tau)$ for each line. To account for residual variations unrelated to reprocessing, including the anomalous line responses discussed in Paper IV, we introduce nuisance parameters that allow time variations in addition to those interpreted as reverberations of the driving light curve. Section 4 presents our velocity–delay maps from MEMECHO analysis of the spectral variations, exhibiting clear signature of an inclined Keplerian disk with a defined outer rim and front/back asymmetry. Section 5 closes with a summary of the main conclusions.

2. PREPSPEC SPECTRAL DECOMPOSITION AND CALIBRATION ADJUSTMENTS

Because subtle features in the reverberating spectrum carry the information of interest, echo mapping analysis can be sensitive to small calibration errors and inaccuracies in error bar estimates. The first stage of our analysis is therefore to fit a simple model decomposing the time-resolved spectra into a mean spectrum plus variable components each with their own root-mean-square (rms) spectrum and light curve. The narrow emission-line components are then used to adjust the photometric calibration and wavelength scale, and to equalise time-dependent spectral resolution. The PREPSPEC code developed and used for this purpose has been helpful in several previous studies (e.g., Grier, et al. 2013) and is available online[1].

2.1. PREPSPEC *Spectral Decomposition*

The main results of our PREPSPEC analysis are given in Fig. 1 for the ultraviolet *HST* spectra and in Fig. 2 for the optical MDM spectra, where the left column gives the mean and rms spectra and the right column the continuum and emission-line light curves.

PREPSPEC's simple model for spectral variations is

$$F(\lambda,t) = A(\lambda) + B(\lambda,t) + C(\lambda,t) \ , \tag{1}$$

where $A(\lambda)$ is the mean spectrum, $B(\lambda,t)$ models the broad emission-line variations, and $C(\lambda,t)$ models continuum variations. We detail these components below.

PREPSPEC decomposes the mean spectrum as

$$A(\lambda) = N(\lambda) + \bar{B}(\lambda) + \bar{C}(\lambda) \ , \tag{2}$$

where $N(\lambda)$ is the NLR spectrum, $\bar{B}(\lambda)$ is the BLR spectrum, and $\bar{C}(\lambda)$ is the continuum. This decomposition is accomplished by using piecewise-cubic spline functions with different degrees of flexibility to separate the various components. The emission-line components are forced to vanish outside a range of velocities around the rest wavelength of each line. For our analysis of NGC 5548 we set the emission-line windows for the NLR lines to ±1500 km s^{-1}, for most of the BLR lines to ±10000 km s^{-1}, and for Hβ to ±6000 km s^{-1}. This decomposition is useful mainly for measuring emission-line strengths, widths, and velocity profiles in the mean spectrum.

PREPSPEC models *variations* in the continuum as a low-order polynomial in log(λ),

$$C(\lambda,t) = \sum_{k=1}^{N_c} C_k(t)\, X(\lambda)^k \ , \tag{3}$$

with N_c coefficients $C_k(t)$ that depend on time. Here

$$X(\lambda) = \frac{\log\left(\lambda^2/\lambda_1\,\lambda_2\right)}{\log\left(\lambda_2/\lambda_1\right)} \tag{4}$$

interpolates linearly in $\log\lambda$ from −1 to +1 over the spectral range λ_1 to λ_2.

PREPSPEC models the broad emission-line variations as

$$B(\lambda,t) = \sum_{\ell=1}^{N_\ell} B_\ell(\lambda)\, L_\ell(t) \ , \tag{5}$$

giving each line ℓ a line profile $B_\ell(\lambda)$ and a light curve $L_\ell(t)$. The line profiles $B_\ell(\lambda)$ are smoothed using spline functions, and set to 0 outside a velocity range centred at the rest wavelength. The light curves are normalised to $\langle L_\ell \rangle = 0$ and $\langle L_\ell^2 \rangle = 1$. This constraint eliminates degeneracy in the model parameters, and lets us interpret $B_\ell(\lambda)$ as the rms spectrum of the variations in line ℓ.

2.2. *UV Spectra from HST*

The UV spectra we analysed are the same *HST* spectra discussed and analyzed with cross-correlation methods in Paper I.

The *HST* spectra exhibit several systems of narrow absorption lines that interfere with our analysis. We used results of spectral modelling analysis (Paper VIII), to identify wavelength regions affected by narrow absorption features, and to divide out these narrow absorption effects. The flux and error bars in these regions are divided by the model transmission restoring to a good approximation the flux that would have been observed in the absence of intervening narrow absorbers, and expanding the error bars appropriately to reflect the lower number of detected photons.

Similarly, a Lorentzian optical depth profile provided an approximate fit to the broad wings of rest-frame geocoronal Lyα absorption. We divided the observed fluxes and their error bars by the model transmission, approximately compensating for the geocoronal Lyα absorption at moderate optical depths. The opaque core of the line was beyond repair, and we omit those wavelengths (1214.3-1216.8Å) from our analysis.

The main results of our PREPSPEC fit to the *HST* spectra are shown in Fig. 1, where the left column shows the spectral and the right column the temporal components of the model.

The top-left panel of Fig. 1 shows the mean spectrum $A(\lambda)$, decomposed into the NLR spectrum $N(\lambda)$ (orange), the BLR spectrum $\bar{B}(\lambda)$ (blue), and continuum $\bar{C}(\lambda)$ (red).

The top-right panel of Fig. 1 shows the continuum light curves, $C(\lambda,t)$, evaluated at five wavelengths across the spectrum. The continuum variations are detected with a median absolute deviation (MAD) of 18% and signal-to-noise (S/N) ratio exceeding 700. The amplitude is larger at 1120 Å on the blue end than at 1720 Å on the red end of the spectrum.

The bottom row of Fig. 1 shows the rms spectra (left) and BLR light curves (right). The blue slope of the F_λ continuum variations is again evident. The strong Lyα and C IV lines exhibit double-peaked profiles in the rms spectra. Variations are detected in N V λ1240 on the red wing of Lyα, in Si IV λ1393, and in He II λ1640.

The BLR light curves generally resemble those of the continuum, but with time delays and other systematic differences that are distinct for each line.

---

[1] http://star-www.st-and.ac.uk/∼kdh1/lib/ps/prepspec.tar.gz

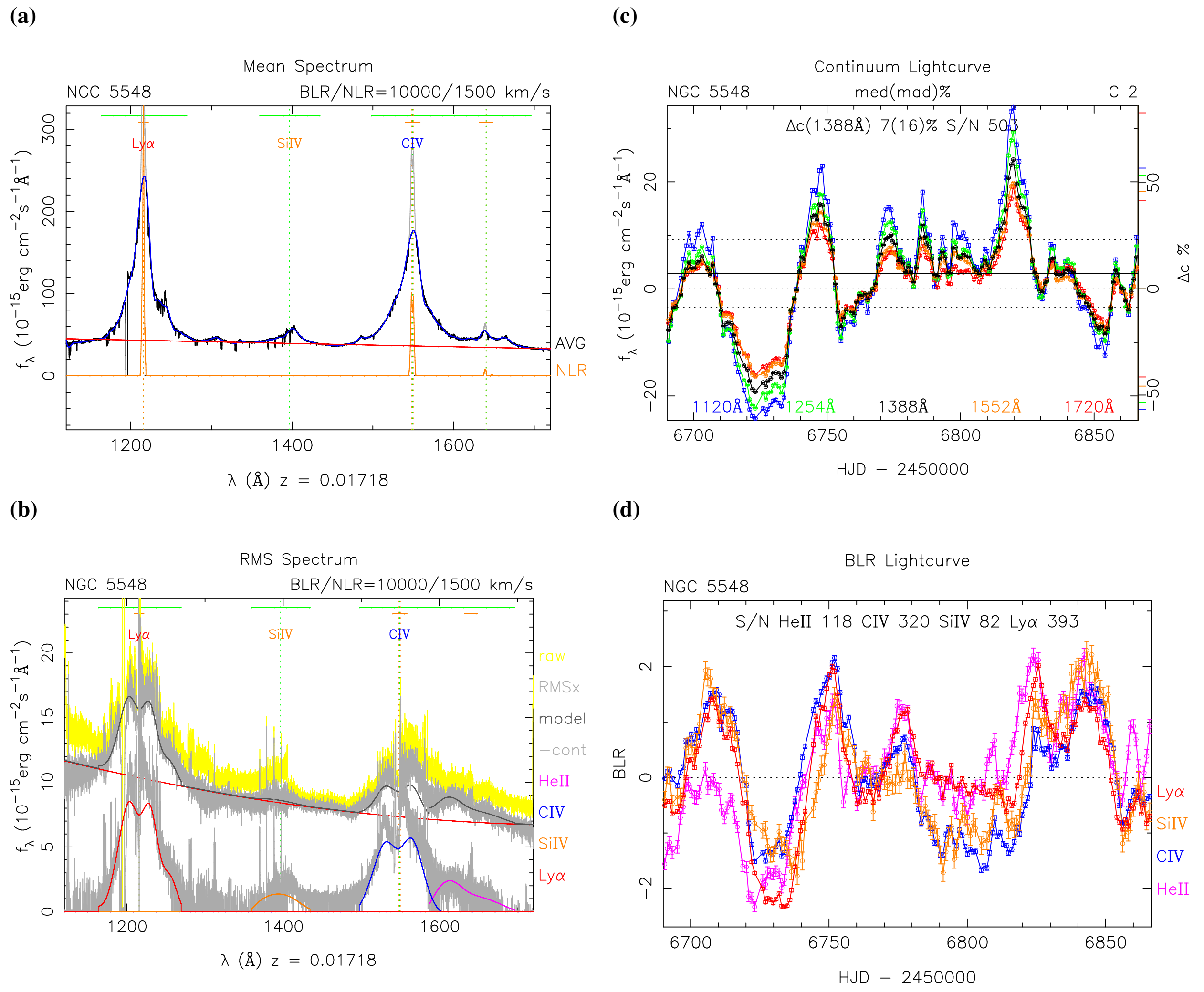

Figure 1. Results of the PREPSPEC fit to *HST* data. Mean (a) and rms (b) spectra. Continuum (c) and emission-line (d) light curves.

2.3. *Optical Spectra from MDM*

Optical spectra from the MDM Observatory were presented and analyzed with cross-correlation analysis in Paper V. Ground-based spectra taken at facilities other than MDM were excluded from this analysis in order to have a consistent and homogeneous dataset taken with the same instrument, same spectral resolution, etc. The ground-based MDM spectra were taken through a 5 arcsec wide slit, and extracted with a 15 arcsec aperture, under variable observing conditions. As a result, each spectrum has a slightly different calibration of flux, wavelength, and spectral resolution. While these residual calibration errors are most evident in the regions around narrow emission lines, they contribute to a smaller extent throughout the spectrum.

To compensate for this, the PREPSPEC model extends to include small adjustments to the calibrations,

$$M(\lambda,t) = p(t)\left(F - \Delta\lambda(t)\,\frac{\partial F}{\partial \lambda} + \Delta s(t)\,\frac{\partial^2 F}{\partial \lambda^2}\right) \ . \qquad (6)$$

Here $p(t)$, $\Delta\lambda(t)$, and $\Delta s(t)$ parameterize small time-dependent adjustments to the photometry, wavelength scale, and spectral resolution. PREPSPEC models $\ln p(t)$ as a low-order polynomial in $\ln\lambda$, ensuring that $p(t)$ remains positive. The median of $p(t)$ is set to unity, since typically a minority of the observed spectra are low due to slit losses and imperfect pointing or variable atmospheric transparency. While PREPSPEC models $\ln p(t)$, $\Delta\lambda(t)$, and $\Delta s(t)$ as low-order polynomials of $\log\lambda$, the wavelength-dependence of these calibration adjustments was not needed over the relatively short wavelength span of the MDM data analyzed here.

2.4. *Patterns in Residuals to the* PREPSPEC *Fit*

Fig. 3 presents results of an analysis of the residuals of the PREPSPEC fit to the ultraviolet *HST* (left) and optical MDM (right) spectra. These provide a visualisation of the evidence for variations in the velocity profiles of the emission lines, and also serve as a check on the success of the absorption line corrections and the calibration adjustments based on the narrow [O III] emission lines, and the accuracy of the error bar estimates.

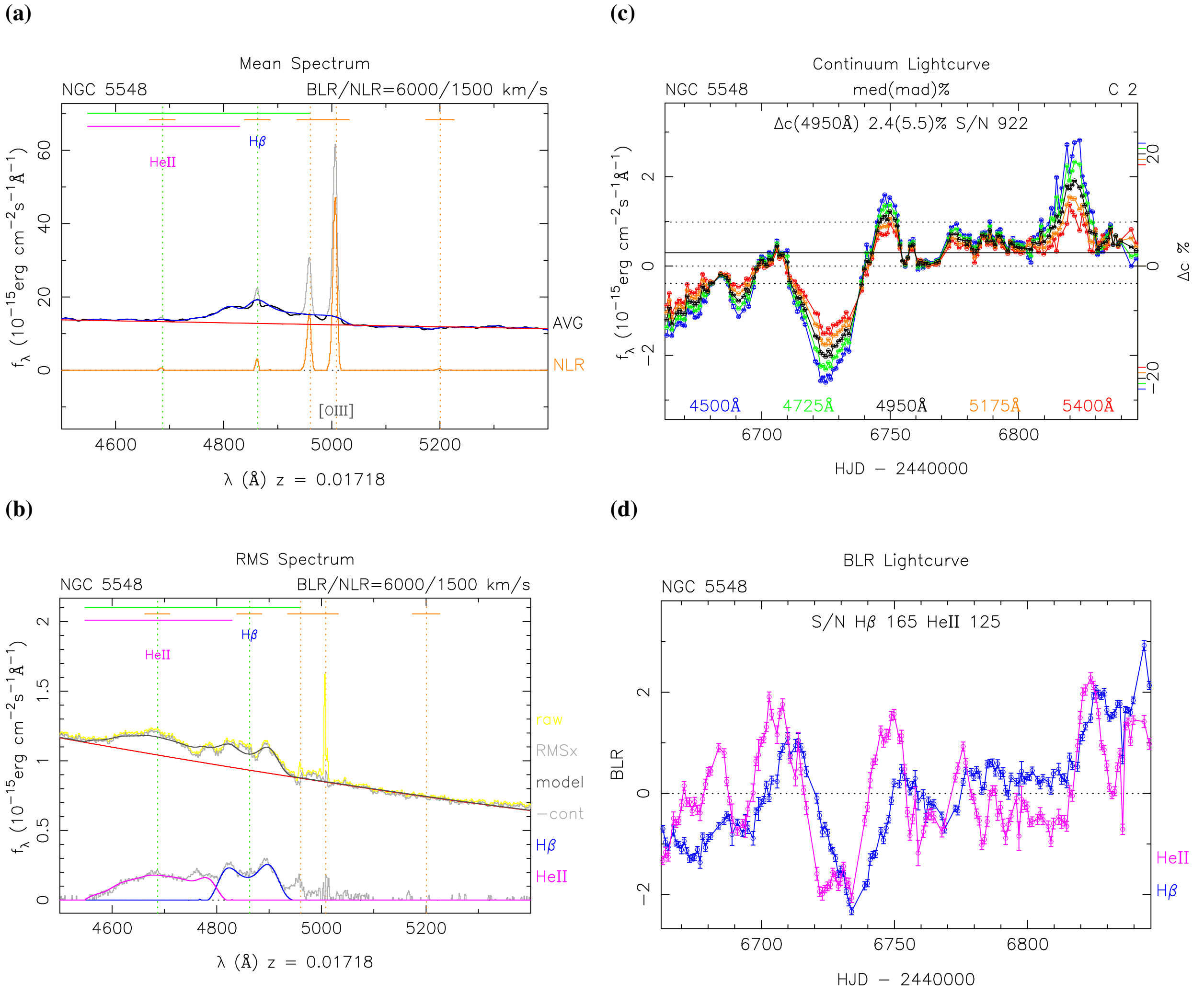

Figure 2. Results of the PREPSPEC fit to MDM data. Mean (a) and rms (b) spectra. Continuum (c) and emission-line (d) light curves.

The upper panels, Fig. 3a and b, present the fitted PREPSPEC model as a greyscale 'trailed spectrogram', with wavelength increasing to the right and time upward. Here horizontal bands arise from the continuum variations and vertical bands mark the locations of emission lines.

The middle panels, Fig. 3c and d, show residuals subtracting the PREPSPEC model from the observed spectra. There are acceptably small fine-scale residuals near the strong narrow [O III] lines at 4593Å and 5008Å, indicating the good quality of the calibration adjustments. In Fig. 3d the evident patterns moving toward the centre of the Hβ line arise from reverberations affecting the line wings first and then moving toward the line centre. We find below that these can be interpreted as reverberation of Hβ-emitting gas with a Keplerian velocity field. There are also stationary features near 4750Å, 4880Å and 4970Å that decrease over the 180-day span of the observations, indicating a gradual decrease in strength of emission at these wavelengths relative to the integrated emission-line flux.

In Fig. 3c the dominant residuals near the C IV line exhibit an intriguing helical 'barber pole' pattern with stripes moving from red to blue across the line profile. This barber pole pattern may be present in the Lyα residuals, but less clearly so due to greater difficulties with absorption line corrections near Lyα. We see no clear evidence of the barber pole pattern in the Hβ residuals, where the residuals are dominated by reverberation signatures. The residual stripes in C IV and Lyα are too strong to be ascribed to calibration errors affecting the *HST* spectra. The barber pole pattern may be interpreted tentatively as evidence for broad azimuthal structures, perhaps due to the shadows of precessing spiral waves on the disk, that rotate around the black hole with a period of ~ 2 yr. The effect must be stronger on the far side to produce features moving from red to blue across the line profile, than on the near side, where they would be seen moving from blue to red. The 2 year period is estimated based on the impression that the stripes move half-way across the C IV profile during the 180 day campaign, so that 180 days is 1/4 of the period of the rotating pattern.

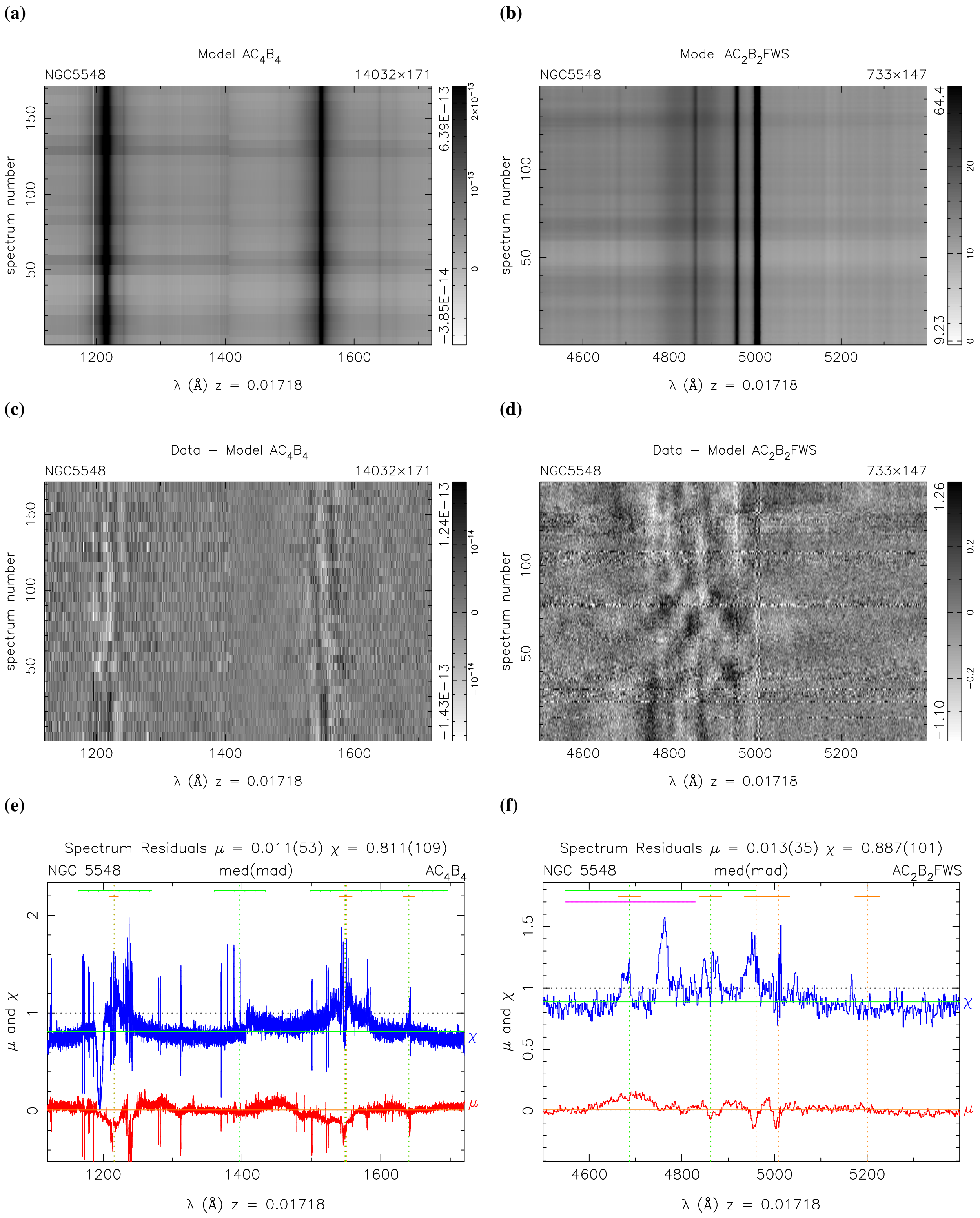

Figure 3. Model (a,b) and residuals (c,d) of the PREPSPEC fit to the *HST* (left) and MDM (right) data. Lower panel shows the mean (red) and rms (blue) over time of the normalised residuals for *HST* (e) and MDM (f). Note in panel (c) the helical "barber pole" pattern of stripes moving from red to blue across the C IV and Lyα line profiles.

The lower panels, Fig. 3e and f, show the mean $\mu(\lambda)$ and rms $\chi(\lambda)$ of the *normalised* residuals, scaled by the error bars. The $\chi(\lambda)$ curves (blue) rise near the emission lines where significant line profile variations are being detected, and level off in the continuum to values below unity, 0.81 for the *HST* and 0.89 for the MDM spectra. These low values indicate that rms residuals are smaller than expected from the nominal error bars. For the MEMECHO analysis to follow, we multiply the nominal error bar spectra by these factors.

3. MEMECHO ANALYSIS: VELOCITY–DELAY MAPPING

Echo mapping assumes that a compact source of ionizing radiation is located at or near the center of the accretion flow. Photons emitted here shine out into the surrounding region, causing local heating and ionization of gas which then emits a spectrum characterized by emission lines as it cools and recombines. Reprocessing times are assumed to be short compared with relevant light-travel times. As distant observers, we see the response from each reprocessing site with a time delay τ from the light-travel time and a Doppler shift v from the line-of-sight velocity. Thus the reverberating emission-line spectrum encodes information about the geometry, kinematics, and ionization structure of the accretion flow.

To decode that information, we interpret observed spectral variations as time-delayed responses to a driving light curve. By fitting a model to the reverberating spectrum $F(\lambda, t)$, we reconstruct a two-dimensional wavelength-delay map $\Psi(\lambda, \tau)$. This effectively slices up the accretion flow on iso-delay surfaces, which are paraboloids co-axial with the line of sight with a focus at the compact source. Each delay slice gives the spectrum of the response, revealing the fluxes and Doppler profiles of emission lines from gas located on the corresponding iso-delay paraboloid. The resulting velocity–delay maps $\Psi(v, \tau)$ provide two-dimensional images of the accretion flow, one for each emission line, resolved on iso-delay and iso-velocity surfaces.

3.1. *Linearized Echo Model*

The full spectrum of ionizing radiation is not observable, and so an observed continuum light curve, $C(t)$, is adopted as a proxy. At each time delay τ, the responding emission-line light curve $L(t)$ is then some non-linear function of the continuum light curve $C(t-\tau)$ shifted to the earlier time $t-\tau$. In addition, the observed line and continuum fluxes include constant or slowly varying background contributions from other light sources, such as narrow-line emission and starlight from the host galaxy. To model these backgrounds and account for the non-linear BLR responses, MEMECHO employs a *linearized* echo model, with reference levels C_0 for the continuum and L_0 for the line flux, and a tangent-curve approximation to variations around these reference levels. Thus the continuum light curve $C(t)$ is decomposed as

$$C(t) = C_0 + \Delta C(t) \ , \tag{7}$$

and the emission-line light curve,

$$L(t) = L_0 + \int \Psi(\tau)\, \Delta C(t-\tau), \mathrm{d}\tau \ , \tag{8}$$

is a convolution of the continuum variations with a delay map $\Psi(\tau)$, giving the one-dimensional delay distribution of the emission-line response.

We find that this linearized echo model fails to provide a good fit to the NGC 5548 data. We therefore generalize the model to allow a time-dependent echo background level, $L_0(t)$.

3.2. *Delay Maps $\Psi(\tau)$ for NGC 5548*

Figure 4 shows the results of our MEMECHO fit to five continuum and six emission-line light curves of NGC 5548. The light curve data are from the PREPSPEC analysis of the *HST* and MDM spectra, described above in Sec. 2. MEMECHO fits all light curves simultaneously, recovering a model for the driving light curve $C(t)$, and for each echo light curve a delay map $\Psi(t)$ and a background light curve $L_0(t)$. The driving light curve $C(t)$ (bottom panel of Fig. 4) is the 1158 Å continuum light curve, with the reference level C_0 (red line) set at the median of the 1158 Å continuum data. Above this are ten echo light curves (right) and corresponding delay maps (left), where the light curve data (black points with green error bars) can be directly compared with the fitted model (blue curves). We model four continuum light curves, at 1300 Å, 1450 Å, and 1700 Å from the *HST* spectra and at 5100 Å from the MDM spectra, as echos of the 1158 Å continuum. The reverberating emission lines are He II λ1640 and He II λ4686, then Hβ and Lyα, and finally Si IV and C IV. The MEMECHO fit accounts for much of the light-curve structure as echos of the driving light curve, but requires significant additional variations (red curves).

Maximum entropy regularization keeps the model light curves and delay maps positive and "as smooth as possible" while fitting the data. The fit shown in Fig. 4 requires $\chi^2/N = 1$ separately for the driving light curve and for each of the echo light curves, where the number of data points are $N = 171$ for the *HST* light curves and $N = 147$ for the MDM light curves. The model light curves (delay maps) are evaluated on a uniform grid of times (delays) spaced by $\Delta t = 0.5$ days, linearly interpolated to the times of the observations. The delay maps span a delay range $0-50$ days. The entropy of each function is measured relative to a default function obtained by gaussian smoothing with full-width-half-maximum of 1, 2 and 4 days for the driving light curve, the delay map, and the echo background, respectively. These choices control the flexibility of the functions.

The delay maps $\Psi(\tau)$ are of primary interest because they indicate the radial distributions from the central black hole over which the continuum and emission-lines are responding to variations in the driving radiation. The continuum light curves exhibit highly correlated variations that are well fit by exponential delay distributions strongly peaked at $\tau = 0$. The median delay, increasing with wavelength, is ~ 1 day at 1700 Å and ~ 5 days at 5100 Å. The echo background

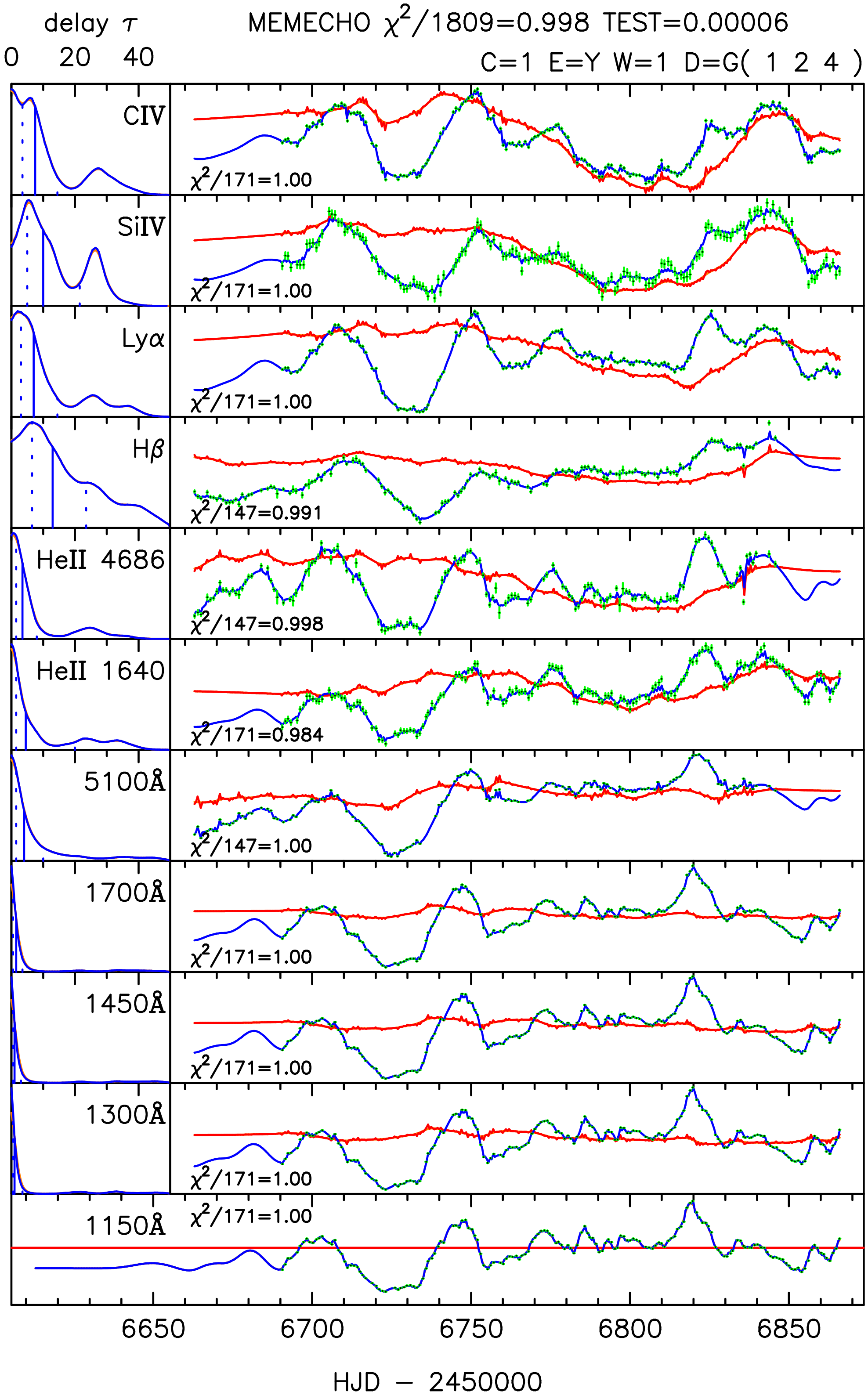

Figure 4. MEMECHO fits to five continuum and six emission-line light curves of NGC 5548. The driving light curve (bottom panel) is the 1158 Å continuum light curve, from *HST* spectra, with a reference level (red line) at the median of the 1158 Å continuum data. Above this are ten echo light curves (right) and corresponding delay maps (left), comparing the light curve data (black points with green error bars) and the echo model (blue curves) with slow background variations (red curves). The echos (bottom up) are four continuum light curves, at 1300 Å, 1450 Å, and 1700 Å from the *HST* spectra and at 5100 Å from the MDM spectra, then six reverberating emission lines, He II λ1640 and λ4686, then Hβ and Lyα and finally Si IV and C IVṪhe MEMECHO fit accounts for much of the light curve structure as echos of the driving light curve, but requires significant additional variations (red curves).

has only small variations, indicating that the linearized echo model is a very good approximation for the continuum light curves.

The emission-line light curves require more extended delay distributions and larger variations in their background levels. The background variations are similar, but not identical, for the six emission-line light curves. The two He II light curves require tight delay distributions peaking at $\tau = 0$, with half the response inside ~ 5 days and 3/4 inside 10 days, and some low-level structure at 20–40 days. The background light curves have a "slow wave" with a 100-day timescale, somewhat different for the two lines, and smaller amplitude 10-day structure. The slow-wave background for He II $\lambda1640$ is rising from HJD[2] 6690 to 6750 while that for He II $\lambda4686$ is more constant. Both backgrounds then decline to minima around HJD 6800 and then rise until 6840. The constant background for He II $\lambda1640$ prior to HJD 6690 and for He II $\lambda4686$ after HJD 6850 is not significant since there are no data during these intervals.

The Hβ response exhibits the most extended delay distribution, with a peak at 7 days, half the response inside 14 days, 3/4 inside 23 days, minor bumps at 25 and 40 days, and falling to 0 at 50 days. The need for this extended delay map is evident in the Hβ light curve, for example to explain the slow Hβ decline following peaks at HJD 6705 and 6745. The Lyα response is more confined than Hβ with a peak at 3 days, half the response inside 7 days, 3/4 inside 15 days, and bumps at 26 and 35 days. Si IV and C IV are similar, with peaks at 5 and 7 days,

The slow-wave backgrounds for all these lines fall slowly from HJD 6740 to 6820 and then rise more rapidly to a peak at HJD 6840. This is the anomalous period discussed in Paper IV, where the emission-lines became weak relative to the continuum. Note also a smaller dip from HJD 6715 to 6790 that deepens the emission-line decline between the two peaks, particularly for C IV. A small peak near HJD 6810 accounts for emission-line peak in C IV, Si IV, and He II $\lambda1640$ that has no clear counterpart in the continum light curves.

Note that the model and background light curves (blue and red curves in Fig. 4) exhibit numerous small spikes in addition to smoother 100-day and 10-day structure. These spikes correspond to data points that are too high or too low, relative to their error bars, to be fit by the smooth default light curve that maximises the entropy. The largest offender is a low point in the Hβ and He II $\lambda4686$ light curves near HJD 6837, which likely represents a calibration error. These outliers could seriously damage the delay maps. The spikes are less prominent if we relax the fit to a higher χ^2/N, but then the fit to the relatively low signal-to-noise ratio Si IV light curve is less satisfactory. Fortunately, because our model has time-dependent backgrounds that can develop sharp spikes where required, the delay maps remain relatively smooth and insensitive to these outliers.

4. VELOCITY–DELAY MAPS

Wavelength–delay maps $\Psi(\lambda,\tau)$ of BLR emission in NGC 5548 are shown as two-dimensional grayscale images in Fig. 5 for the MEMECHO fit to the optical spectra from MDM, and in Fig. 6 for the UV spectra from *HST*. To the right are the projections $\Psi(\tau)$ giving delay maps for the full wavelength range (black) and for velocity ranges centered on the rest wavelengths of the emission lines, as indicated by the colored bars above and below the grayscale map. Below the projections $\Psi(\lambda)$ give the spectrum of the full response (black) and of the response in four delay ranges, 0–5 days (purple), 5–10 days (green), 10–15 days (orange), and 15–20 days (red). Velocity–delay maps centered on the six emission lines are presented in Fig. 7. These two-dimensional maps show that the emission-line response inhabits the interior of a virial envelope (orange dashed), and exhibit structure indicating an inclined Keplerian disk, $i = 45°$, with an outer rim at $R/c = 20$ days, as discussed below. These maps and their interpretation are the main results of interest emerging from our MEMECHO analysis.

Details from the MEMECHO fit are shown in Figs 8 and 9 for the *HST* and MDM spectra, respectively, with the same format as in Fig 4. The fit models as echoes the same four continuum light curves, at 1350 Å, 1450 Å, 1700 Å, and 5100 Å, and now as well the continuum-subtracted emission-line variations across the full wavelength range of the *HST* and MDM spectra. The PREPSPEC model provided the variable continuum model that was subtracted to isolate the BLR spectra used in the MEMECHO fit. As before, the proxy driving light curve $C(t)$ is the continuum light curve at 1158 Å. The model allows echo responses over a delay range 0–50 days, and includes a time-variable background spectrum $L_0(\lambda,t)$. This allows the model to account for the period of anomalous line response during the 'BLR holiday' (Paper IV), as well as other features in the data, real or spurious, that are not easily interpretable in terms of the linearized echo model.

The entropy now steers the fit toward models with smooth spectra as well as smooth light curves and delay maps. We actually construct a series of MEMECHO maps that fit the data at different values of χ^2/N, ranging from 5 to 1. At higher χ^2, the fit to the data is poor and the maps are smooth. At lower χ^2, the fit improves and the maps develop more detailed structure. When χ^2 is too low the fit becomes strained as the the model strives to fit noise features, e.g., by introducing spikes in the gaps between data points in the driving light curve. The fits and maps shown here for a fit with $\chi^2/N = 1.2$ is a good compromise between noise and resolution. Our tests show that the main features interpreted here are robust to changes in the control parameters of the fit. These parameters adjust the relative "stiffness" of the driving lightcurve, the background lightcurve, the echo maps, and the aspect ratio of resolution in the velocity vs delay directions.

From Figs. 5 and 6, the three strongest lines — Lyα, C IV, and Hβ — have a similar velocity-delay structure, with most of their response between 5 days and 15 days. To first order,

---

[2] HJD as used here refers to the four least significant digits of the heliocentric Julian date.

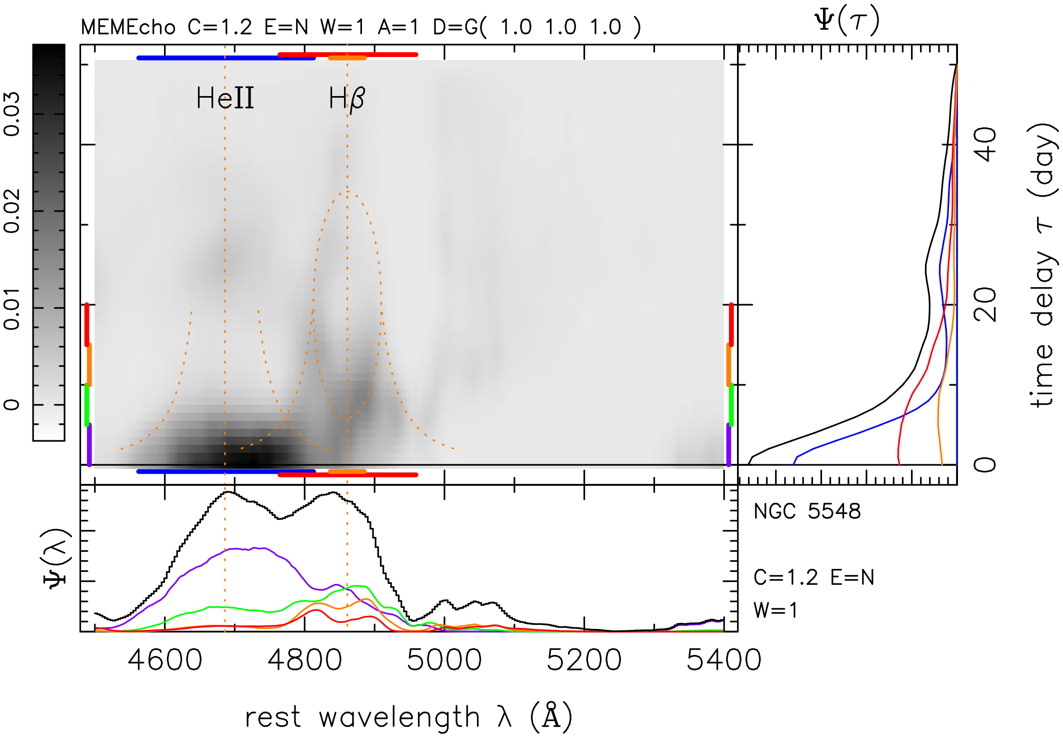

Figure 5. Two-dimensional wavelength–delay map $\Psi(\lambda,\tau)$ reconstructed from the MEMECHO fit to the optical spectra from MDM. Delays are measured relative to the 1158 Å continuum light curve. Projections below and to the right of the grayscale map give the projections $\Psi(\lambda)$ and $\Psi(\tau)$. Dashed orange curves show the envelope around each line inside which emission can occur from a Keplerian disk inclined by $i = 45^\circ$ orbiting a black hole of mass $M_{\rm BH} = 7 \times 10^7\, M_\odot$. The ellipse shown for Hβ corresponds to disk radius at $R/c = 20$ days.

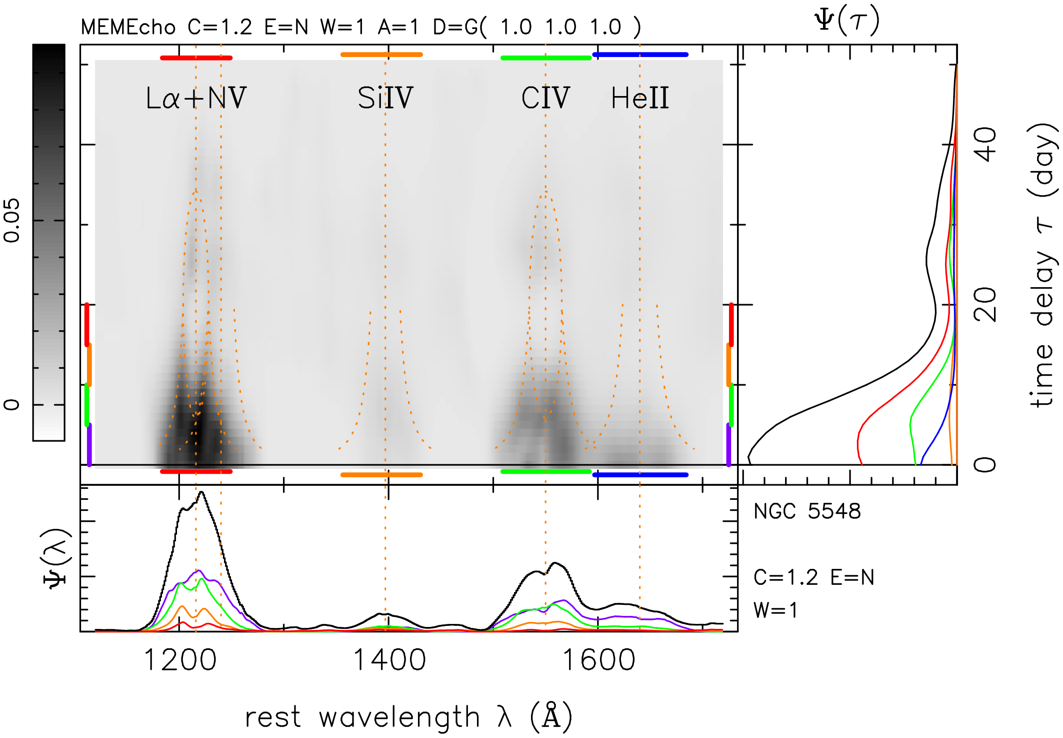

Figure 6. Two-dimensional wavelength–delay map $\Psi(\lambda,\tau)$ reconstructed from the MEMECHO fit to the ultraviolet spectra from *HST*. Delays are measured relative to the 1158 Å continuum light curve. Projections below and to the right of the grayscale map give the projections $\Psi(\lambda)$ and $\Psi(\tau)$. Dashed orange curves show the envelope around each line inside which emission can occur from a Keplerian disk inclined by $i = 45^\circ$ orbiting a black hole of mass $M_{\rm BH} = 7 \times 10^7\, M_\odot$. Ellipses shown for Ly$\alpha$ and C IV correspond to disk radius $R = 20$ light days.

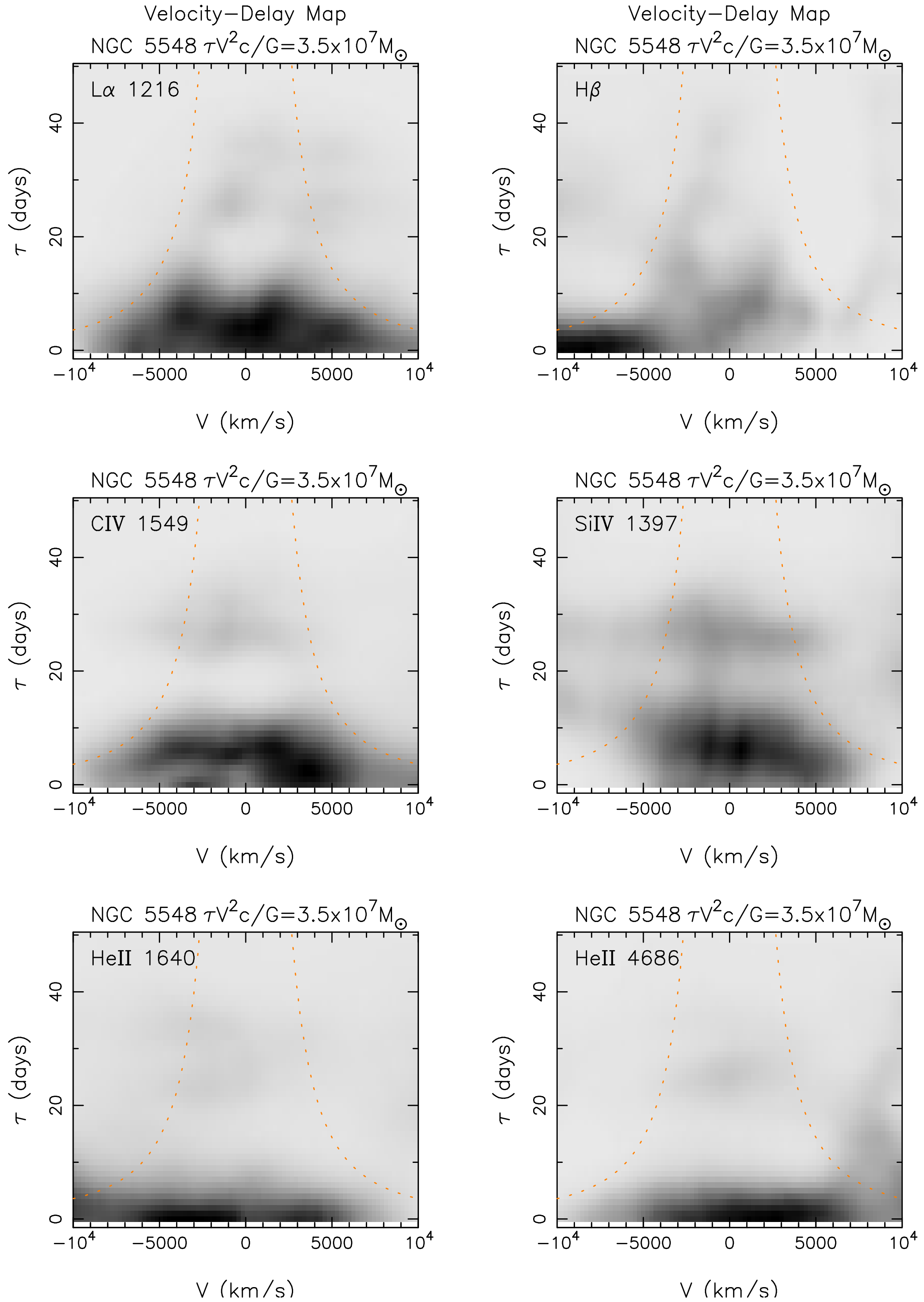

Figure 7. Velocity-delay maps $\Psi(v,\tau)$ reconstructed from the MEMECHO fit to the *HST* and MDM spectra. Delays are measured relative to the 1158 Å continuum light curve. Dashed orange curves show the virial envelope around each line inside which emission can occur from a Keplerian disk inclined by $i = 45^\circ$ orbiting a black hole of mass $M_{\rm BH} = 7 \times 10^7\, M_\odot$.

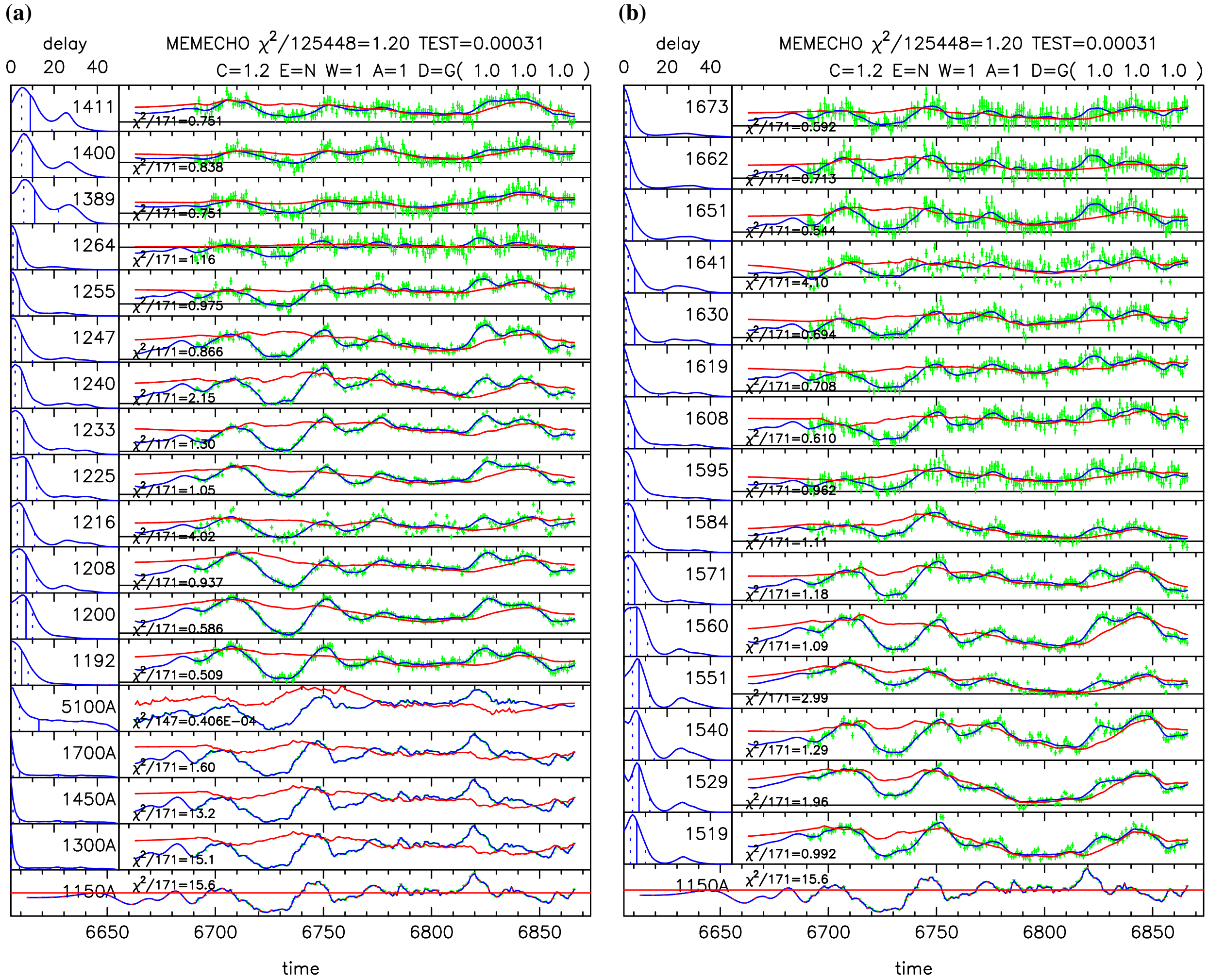

Figure 8. Details of the MEMECHO fit to spectral variations in the *HST* data. light curve data with error bars (green) are compared with the fitted model (blue) and varying background (red). The lower panel exhibits the driving light curve at 1158 Å. Above this are delay maps (left) and echo light curves (right) for continuum echos at 1300 Å, 1450 Å, 1700 Å and 5100 Å, and for selected wavelengths including (a) Lyα λ1216, N V λ1240, and Si IV λ1393, and (b) C IV λ1549 and He II λ1640.

the response in all three lines is red-blue symmetric. This indicates that radial motions are sub-dominant in the BLR, as a strong inflow (outflow) component would produce shorter delays on the red (blue) side of the velocity profile (Welsh & Horne 1991).

The He II response is largely inside 5 days, and extends to $\pm 10{,}000$ km s^{-1}, compatible with expected radial ionization structure, and virial motions. In Fig. 5, we see that He II response is broad and single peaked. He II dominates the Hβ response in the 0-5-day delay slice (purple), becomes sub-dominant at 5–10 days (green), and almost negligible at larger delays. The He II λ1640 and He II λ4686 delay ranges and velocity structures are similar. There is no signature of a double-peaked structure in these two lines.

In Fig. 5, the Hβ delay map $\Psi(\tau)$ for the full profile ($\pm$6000 km s^{-1}, red) and for the line core ($\pm$1500 km s^{-1}, orange) is flat or rising from 0–10 days, then tails away. The Hβ response spectrum $\Psi(\lambda)$ exhibits a double-peaked structure in the 10–15 days (orange) and 15–20 days (red) delay ranges, the peaks separated by $\sim$ 5000 km s^{-1}. In the 5-10-day slice, the Hβ response has a central peak flanked by ledges that extend to $\pm$5000 km s^{-1}. Fig. 6 shows similar double-peaked response in Lyα and somewhat less clearly in C IV.

Clearly recognizable in the velocity–delay structure is the signature of an inclined Keplerian disk with a well-defined outer edge. The velocity-delay maps provide a plausible interpretation for the "M"-shaped structure of lag vs. velocity seen in the cross-correlation results (Papers I and V). The outer edges of the "M" arise from the virial envelope. The "U"-shaped interior of the "M" dips down from 20 days to 5 days, and we interpret this as the lower half of an ellipse in the velocity–delay plane, which is the signature of a ring of gas orbiting the black hole at radius $R = 20$ light days.

The Hβ response exhibits the clearest signature of an ellipse in the velocity–delay plane, corresponding to an annu-

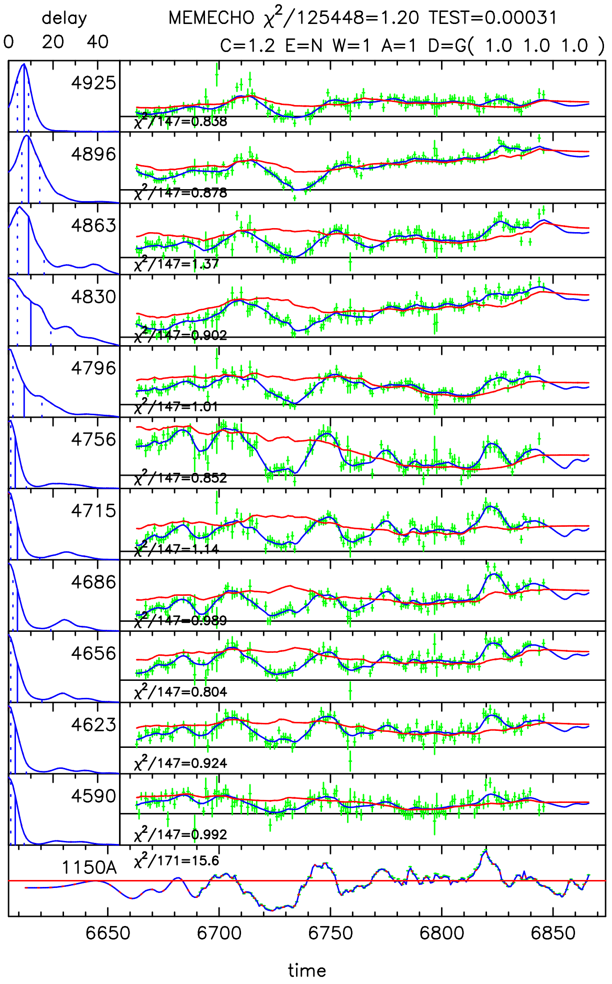

Figure 9. Details of the MEMECHO fit to spectral variations in the MDM data. light curve data with error bars (green) are compared with the fitted model (blue) and varying background (red). The lower panel exhibits the driving light curve at 1158 Å. Above this are delay maps (left) and echo light curves (right) for continuum echos at 1300 Å, 1450 Å, 1700 Å, and 5100 Å, and for selected wavelengths including He II λ1640, and Hβ λ4861.

lus in the Keplerian disk. The (stronger) near side of the annulus has a delay at $\tau = (R/c)(1-\sin i) \approx 5$ days and the (weaker) far side extends to $\tau = (R/c)(1+\sin i) \sim 35$ days Assuming a thin disk, the ratio gives $\sin i \approx 0.75$, or $i \approx 45^\circ$. The double-peaked velocity structure at $\tau \approx 20$ days then gives the black hole mass. The framework shown by dashed orange curves on the plot, adjusted by eye to fit the main features, is for black hole mass $M_{\rm BH} = 7\times10^7\ M_\odot$, $i = 45^\circ$, and $R_{\rm out} = 20$ light days.

The velocity–delay structure also indicates a stronger response from the near side than from the far side of the inclined disk. We see the upper half of the ellipse only faintly in the velocity–delay map of Hβ and perhaps also the Lyα. The C IV map and (less reliable) Si IV map show a faint response at 25–30 days that is not very clearly connected to the stronger response inside 10–15 days. If the response structure were azimuthally symmetric, the upper and lower halves of the ellipse would be more equally visible. The mean delay averaged around the ellipse would be $R/c \sim 20$ days, and this is similar to typical Hβ lags seen in the past. The much shorter lags in the STORM data may be interpreted as due at least in part to an anisotropy present in 2014 that was usually much weaker or absent during previous monitoring campaigns. The near/far contrast ratio can be determined by more careful modelling.

4.1. *Comparison with velocity-delay maps at other epochs*

In 2015 Jan-Jul, a year after our campaign, NGC 5548 was monitored with the Yunnan Faint Object Spectrograph and Camera on the 2.4 m telescope at Lijiang, China, resulting in 61 good spectra over 205 days that provide the basis for a MEM analysis yielding a velocity-delay map for Hβ (Xiao, et al. 2018). This 2015 map exhibits structure remarkably similar to that seen in our 2014 map, including the virial envelope, the 'M'-shaped structure with $\tau \sim 10$ d and $V \sim \pm2400$ km s^{-1} at the peaks of the 'M', and a well defined ellipse extending out to $\tau \sim 40$ d.

(Xiao, et al. 2018) also present Hβ velocity-delay maps constructed from 13 annual AGNWatch campaigns 1989-2001. While several of these maps show hints of a ring-like structure, the quality of these maps is much lower due to less intensive time sampling, making it difficult to be confident about the information that they may be able to convey.

In combination, the high-fidelity 2014 and 2015 Hβ velocity-delay maps each show a clear virial envelope and distinct ellipse centred at 20 light days. Thus the Hβ response arises from a Keplerian disc with a relatively sharp outer rim at 20 light days that remained stable for an interval of at least a year. In 2014 the response is weak on the top of the velocity-delay ellipse. In 2015 the response is clearly visible on the blue side and over the top of the velocity-delay ellipse, and relatively weak on the red side. This indicates significant azimuthal modulation of the response that evolves, perhaps rotates, on a timescale of 1 year. Future velocity-delay mapping experiments to monitor this strucure could be interesting to elucidate its origin and implications.

5. SUMMARY

In this contribution, we achieve the primary goal of the AGN STORM campaign by recovering velocity-delay maps, which are the key to understanding the geometry, ionization structure, and kinematics of the broad-line region, for the prominent broad emission lines, Lyα, C IV, He II and Hβ, in the spectrum of NGC 5548.

Our analysis interprets the ultraviolet *HST* spectra (Paper I) and optical MDM spectra (Paper V) secured in 2014 during the 6-month STORM campaign on NGC 5548. This dataset provides spectrophotometric monitoring of NGC 5548 with unprecedented duration, cadence, and signal-to-noise ratio suitable for interpretation in terms of reverberations in the broad emission-line regions (BLR) surrounding the black hole. Assuming that the time delays arise from light travel time, the velocity-delay maps we construct from the reverberating spectra provide 2-dimensional images of the BLR, one for each line, resolved on iso-delay paraboloids and line-of-sight velocity.

We used absorption line modelling results from Paper VIII to divide out absorption lines affecting the *HST* spectra. We used PREPSPEC to re-calibrate the flux, wavelength, and spectral resolution in the optical MDM spectra using the strong narrow emission lines as internal calibrators. Residuals of the PREPSPEC fit indicate the success of the calibration adjustments, and provide a basis for adjusting the error bar spectra by 10-20%.

The linearised echo model that we normally use for echo mapping is violated in the STORM dataset by anomalous emission-line behavior, the 'BLR holiday' discussed in Paper IV. We model this adequately as a slowly varying background spectrum superimposed on which are the more rapid variations due to reverberations.

Residuals of the PREPSPEC fit reveal significant emission-line profile changes. Features are evident moving inward from both red and blue wings toward the center of the Hβ line, interpretable as reverberations of a BLR with a Keplerian velocity field.

A helical 'barber pole' pattern with stripes moving from red to blue the across line profile is evident in the C IV and possibly also the Lyα line, suggesting azimuthal structure rotating with a period of ~ 2 yr around the far side of the accretion disk. This may be interpreted tentatively as precession or orbital motion of disk structures. Further *HST* observations of NGC 5548 over a multi-year timespan but with a cadence of perhaps 10 days rather than 1 day, could be important to investigate the persistence or transience and ultimately the nature of this new AGN phenomenon.

We use the PREPSPEC fit to extract lightcurves for lines and continua and use MEMECHO to fit these echo lightcurves with the 1158 Å continuum lightcurve serving as a proxy for the driving lightcurve. The MEMECHO fit determines a set of echo maps $\Psi(\tau)$ giving the delay distribution of each echo, effectively slicing up the reverberating region on iso-delay paraboloids. The structure in these echo maps indicates radial stratification, with He II responding from inside 5 light days, and the Lyα C IV and Hβ response extending out to or beyond 20 light days.

By using MEMECHO to fit reverberations in the emission-line profiles, we construct velocity-delay maps $\Psi(v,\tau)$ that resolve the BLR in time delay and line-of-sight velocity. The BLR response is confined within a virial envelope around each line, with double-peaked velocity profiles in the response in 10-20 day delay slices. The 'M'-shaped delay vs velocity structure found using velocity-resolved cross-correlation lags in Papers I and V are seen here to be the signature of a Keplerian disk. The outer legs of the M arise from the virial envelope between 5 and 20 days, the inner U of the M is the lower part of an ellipse extending from 5 to 35 days. This velocity-delay structure is most straightforwardly interpreted as arising from a Keplerian disk extending from $R/c = 5$ to 20 days, inclined by 45°, centred on a black hole of mass $7 \times 10^7\ M_\odot$. The BLR has a well-defined outer rim at $R/c = 20$ days, but the far side of the rim may be obscured or less responsive than the near side.

Detailed modelling of the STORM data, guided by the features in the velocity-delay maps presented here, should be able to refine and quantify uncertainties on these features of the BLR, the inclination, and the black hole mass.

ACKNOWLEDGEMENTS

Support for *HST* program number GO-13330 was provided by NASA through a grant from the Space Telescope Science Institute, which is operated by the Association of Universities for Research in Astronomy, Inc., under NASA contract NAS5-26555. K.H. acknowledges support from STFC grant ST/R000824/1. G.D.R., B.M.P., M.M.F, C.J.G., and R.W.P. are grateful for the support of the National Science Foundation through grant AST-1008882 to The Ohio State University. A.J.B. and L.P. have been supported by NSF grant AST-1412693. M.C. Bentz gratefully acknowledges support through NSF CAREER grant AST-1253702 to Georgia State University. S.B. is supported by NASA through the Chandra award no. AR7-18013X issued by the Chandra X-ray Observatory Center, operated by the Smithsonian Astrophysical Observatory for and on behalf of NASA under contract NAS8-03060. S.B. was also partially supported by grant HST-AR-13240.009. M.C. Bottorff acknowledges HHMI for support through an undergraduate science education grant to Southwestern University. E.M.C., E.D.B., L.M., and A.P. acknowledge support from Padua University through grants DOR1699945/16, DOR1715817/17, DOR1885254/18, and BIRD164402/16. G.F. and M. Dehghanian acknowledge support from the NSF (AST-1816537), NASA (ATP 17-0141), and STScI (HST-AR-13914, HST-AR-15018), and the Huffaker Scholarship. K.D.D. is supported by an NSF Fellowship awarded under grant AST-1302093. R.E. gratefully acknowledges support from NASA under the ADAP award 80NSSC17K0126. P.A.E. acknowldges UKSA support. A.V.F.'s group at UC Berkeley is grateful for financial assistance from NSF grant AST-1211916, the TABASGO Foundation, and the Christopher R. Redlich Fund. J.M.G. gratefully acknowledges support from NASA under awards NNX15AH49G and 80NSSC17K0126. P.B.H. is supported by NSERC. M.I. acknowledges support from the National Research Foundation of Korea (NRF) grant, No. 2017R1A3A3001362. M.D.J. acknowledges NSF grant AST-0618209. M.K. was supported by the National Research Foundation of Korea (NRF) grant funded by the Korea government (MSIT) (No. 2017R1C1B2002879). SRON is financially supported by NWO, the Netherlands Organization for Scientific Research. C.S.K. acknowledges the support of NSF grant AST-1009756. Y.K. acknowledges support from DGAPA-PAIIPIT grant IN106518. D.C.L. acknowledges support from NSF grants AST-1009571 and AST-1210311. P.L. acknowledges support from Fondecyt grant #1120328. A.P. is supported by NASA through Einstein Postdoctoral Fellowship grant number PF5-160141 awarded by the Chandra X-ray Center, which is operated by the Smithsonian Astrophysical Observatory for NASA under contract NAS8-03060. J.S.S. acknowledges CNPq, National Council for Scientific and Technological Development (Brazil) for partial support and The Ohio State University for warm hospitality. T.T. has been supported by NSF grant AST-1412315. T.T. and B.C.K. acknowledge support from the Packard Foundation in the form of a Packard Research Fellowship to T.T. The American Academy in Rome and the Observatory of Monteporzio Catone are thanked by T.T. for kind hospitality. The Dark Cosmology Centre is funded by the Danish National Research Foundation. M.V. gratefully acknowledges support from the Danish Council for Independent Research via grant no. DFF 4002-00275. J.-H.W. acknowledges support by the National Research Foundation of Korea (NRF) grant funded by the Korean government (No. 2010-0027910). This research has made use of the NASA/IPAC Extragalactic Database (NED), which is operated by the Jet Propulsion Laboratory, California Institute of Technology, under contract with the National Aeronautics and Space Administration.

REFERENCES

Baldwin, J.A., et al. 1995, ApJ, 455, L119

Barth, A.J., et al. 2015, ApJS, 217, 26

Bentz, M.C., & Katz, S. 2015, PASP, 127, 67

Bentz, M.C., Peterson, B.M., Netzer, H., Pogge, R.W., & Vestergaard, M. 2009, ApJ, 697, 160

Bentz, M.C., et al. 2006, ApJ, 644, 133

—. 2007, ApJ, 662, 205

—. 2010a, ApJ, 716, 993

—. 2010b, ApJL, 720, 46

—. 2013, ApJ, 767:149

Blandford, R. D., & McKee, C. F. 1982, ApJ, 255, 419

Bottorff, M., Korista, K.T., Shlosman, I., & Blandford, R.D. 1997, ApJ, 479, 200

Brewer, B.J. , Treu, T., Pancoast, A., Barth, A.J., Bennert, V.N., Bentz, M.C., Filippenko, A.V., Greene, J.E., Malkan, M.A., Woo, J.-H. 2011, ApJ, 733, L33

Cackett, E.M., & Horne, K. 2006, MNRAS, 365, 1180

Cackett, E.M., Horne, K., & Winkler, H. 2007, MNRAS, 380, 669

Capriotti, E.R., Foltz, C.B., & Byard, P.L. 1980, ApJ, 241, 903

Cardelli, J. A., Clayton, G. C., & Mathis, J. S. 1989, ApJ, 345, 245

Clavel, J., Wamsteker, W., & Glass, I.S. 1989, ApJ, 337, 236

Clavel, J., et al. 1990, MNRAS, 246, 668

—. 1991, ApJ, 366, 64

Collier, S. J., et al. 1998, ApJ, 500, 162

—. 2001, ApJ, 561, 146

Crenshaw, D.M., & Kraemer, S.B. 1999, ApJ, 521, 572

Crenshaw, D.M., et al. 1996, ApJ, 470, 322

—. 2009, ApJ, 698, 281

De Rosa, G., Peterson, B.M., Ely, J., et al. 2015, ApJ, 810:128 (Paper I)

De Rosa, G., Venemans, B. P., Decarli, R., Gennaro, M., Simcoe, R. A., Dietrich, M., Peterson, B. M., Walter, F., Frank, S., McMahon, R. G., Hewett, P. C., Mortlock, D. J., & Simpson, C. 2014, ApJ, 790:145

Denney, K.D., et al. 2009, ApJ, 704, L80

—. 2010, ApJ, 721, 715

—. 2014, ApJ, 796:134

Done, C., & Krolik, J,H. 1996, ApJ, 463, 144

Edelson, R., Gelbord, J.M., Horne, K., et al., ApJ, 810:129 (Paper II)

Elvis, M. 2004, ASP Conf. Series, Vol. 311, p. 109

Ely, J., Massa, D., Ake, T., Beland, S., Penton, S., Oliveira, C., Proffitt, C., Sahnow, D. 2011, COS FUV Gridwire Flat Field Template, Instrument Science Report COS 2011-03 (Baltimore: STScI)

Eracleous, M., & Halpern, J.P. 1994, ApJS, 90, 1

—. 2003, ApJ, 599, 886

Everett, J.E. 2003, ASP Conf. Series, Vol. 290, p. 199

Fausnaugh, M.M., Denney, K.D., Barth, A.J., et al. 2016, ApJ, 821:56 (Paper III)

Gardner, E., & Done, C. 2017, MNRAS, 470, 2245

Gehrels, N., 1986, ApJ, 303, 336

Gehrels, N., et al. 2004, ApJ, 611, 1005

Gezari, S., Halpern, J.P., & Eracleous, M. 2007, ApJS, 169, 167

Goad, M.R., Korista, K.T., De Rosa, G., et al., ApJ, 824:11 (Paper IV)

Green, J.C., et al. 2012, ApJ, 744:60

Greene, J.E., & Ho, L.C. 2005, ApJ, 630, 122

Grier, C.J., Peterson, B.M., Horne, K., et al. 2013, ApJ, 764:47

Grupe, D. & Mathur, S. 2004, ApJ, 606, L41

Guerras, E., Mediavilla, E., Jimenez-Vicente, J., Kochanek, C. S., Muñoz, J. A., Falco, E., & Motta, V. 2013, ApJ, 764:160

Hamann, F., & Sabra, B. 2004, ASP Conf. Series Vol. 311, p. 203

Hernandez, S., et al. 2014, STIS Instrument Handbook, Version 13.0 (Baltimore: STScI)

Holland, S.T., et al. 2014, Cosmic Origins Instrument Handbook, Version 6.0 (Baltimore: STScI)

Horne, K. 1994, in Astronomical Society of the Pacific Conference Series, Vol. 69, Reverberation Mapping of the Broad-Line Region in Active Galactic Nuclei, ed. P. M. Gondhalekar, K. Horne, & B. M. Peterson, pp. 23–51

Horne, K., Peterson, B.M., Collier, S.J., & Netzer, H., 2004, PASP, 116, 465

Horne, K., Welsh, W.F., & Peterson, B.M. 1991, ApJ, 367, L5

Jarvis, M.J., & McLure, R.J. 2006, MNRAS, 369, 182

Kaastra, J., et al. 2014, Science, 345, 64

Kaspi, S., Brandt, W.N., Maoz, D., Netzer, H., Schneider, D.P., & Shemmer, O. 2007, ApJ, 659, 997

Kaspi, S., Maoz, D., Netzer, H., Peterson, B.M., Vestergaard, M., & Jannuzi, B.T., 2005, ApJ, 629, 61

Kaspi, S., & Netzer, H. 1999, ApJ, 524, 71

Kaspi, S., Smith. P.S., Netzer, H., Maoz, D., Jannuzi, B.T, & Giveon, U. 2000, ApJ, 533, 631

Kelly, B. C., Bechtold, J., & Siemiginowska, A. 2009, ApJ, 698, 895

Kollatschny, W. 2003, A&A, 407, 461

Kollmeier, J., et al. 2006, ApJ, 648, 128

Komatsu, E., et al. 2011, ApJS, 192, 18

Korista, K.T., et al. 1995, ApJS, 97, 285

Korista, K.T., & Goad, M.R. 2000, ApJ, 586, 234

Kozłowski, S., et al. 2010, ApJ, 708, 927

Kriss, G.A., et al. 2011, A&A, 534, 41

Kriss, G.A., De Rosa, G., Ely, J., Peterson, B.M., et al. 2018, ApJ, in prep.

Krolik, J.H., et al. 1991, ApJ, 371, 541

Krongold, Y., Nicastro, F., Brickhouse, N.S., Elvis, M. & Mathur, S. 2005, ApJ, 622, 842

Krongold, Y., Nicastro, F., Elvis, M., Brickhouse, N.S., Binette, L., Mathur, S., & Jiménez-Bailó, E. 2007, ApJ, 659,1022

Lewis, K.T., Eracleous, M., & Storchi-Bergmann, T. 2010, ApJS, 187, 416

Mathur, S., Gupta, A., Page, K., Pogge, R.W., Krongold, Y., Goad, M.R., et al., 2017, ApJ, 846, 55.

Massa, D., Ely, J., Osten, R., Penton, S., Aloisi, A., Bostroem, A., Roman-Duval, J., & Proffitt, C. 2014, Updated Absolute Flux Calibration of the COS FUV Modes, Instrument Science Report COS 2013-09 (Baltimore: STScI)

MacLeod, C. L., et al. 2010, ApJ, 721, 1014

—. 2012, ApJ, 753, 106

Marconi, A., Axon, D.J., Maiolino, R., Nagao, T., Pastorini, G., Pietrini, P., Robinson, A., & Torricelli, G. 2008, ApJ, 678, 693

Mathur, S., & Grupe, D. 2005, A&A, 432, 463

McLure, R.J., & Jarvis, M.J. 2002, MNRAS, 337, 109

McGill, K.L., et al. 2008, ApJ, 673, 703

M^{c}Hardy, I.M., Cameron, D.T., Dwelly, T., Connolly, S., Lira, P., Emmanoulopoulos, D., Gelbord, J., Breedt, E., Arévalo., P. & Uttley, P. 2014, MNRAS, 444, 1469

Murray, N., & Chiang, J. 1997, ApJ, 474, 91

Netzer, H., & Marziani, P. 2010, ApJ, 724, 318

Netzer, H., & Trakhtenbrot, B. 2014, MNRAS, 438, 672

O'Brien, P.T., et al. 1998, ApJ, 509, 163

Pancoast, A., Brewer, B.J., Treu, T., Park, D., Barth, A.J., Bentz, M.C., & Woo, J.-H. 2014, MNRAS, 445, 3073

Pancoast, A., et al. 2012, ApJ, 754, 49

Pancoast, A., et al. 2014, MNRAS, 445, 3073

Park, D., Kelly, B. C., Woo, J.-H., & Treu, T. 2012a, ApJS, 203, 6

Park, D., Woo, J.-H., Bennert, V. N., Treu, T., Auger, M. W., & Malkan, M. A., 2015, ApJ, 799, 164

Park, D., Woo, J.-H., Denney, K.D., & Shin, J., 2013, ApJ, 770:87

Park, D., Woo, J.-H., Treu, T., et al. 2012, ApJ, 747, 30

Pei, L., Fausnaugh, M.M., Barth, A.J., et al. 2017, ApJ, 837, 131 (Paper V)

Peterson, B.M. 1993, PASP, 105, 247

—. 2014, Space Sci. Rev., 183, 253

Peterson, B.M., & Wandel, A. 1999, ApJL, 521, L95

— . 2000, ApJL, 540, L13

Peterson, B.M., Wanders, I., Horne, K., Collier, S., Alexander. T., Kaspi, S., & Maoz, D. 1998, PASP, 110, 660

Peterson, B.M., et al. 2002, ApJ, 581, 197

—. 2004, ApJ, 613, 682

—. 2005, ApJ, 641, 638

—. 2013, ApJ, 779:109

—. 2014, ApJ, 795:149

Proga, D., et al. 2000, ApJ, 543, 686

Reichert, G.A., et al. 1994, ApJ, 425, 582

Rodríguez-Pascual, P.M., et al. 1997, ApJS, 110, 9

Salviander, S., Shields, G.A., Gebhardt, K., & Bonning, E.W. 2007, ApJ, 662, 128

Sahnow, D, et al. 2011, SPIE, 8145, 0

Schlafly, E.F., & Finkbeiner, D.P 2011, ApJ, 737:103

Schlegel, D. J., Finkbeiner, D. P., & Davis, M. 1998, ApJ, 500, 525

Scott, A.E., Brandt, W.N., Behar, E., Crenshaw, D.M., Gabel, J.R., Gibson, R.R., Kaspi, S., Kraemer, S.B., & Turner, T.J. 2014, ApJ, 797:105

Sergeev, S.G., Doroshenko, V.T., Golubinskiy, Yu. V., Merkulova, N.I., & Sergeeva, E.A. 2005, ApJ, 622, 129

Sergeev, S.G., Doroshenko, V.T., Dzyuba, S.A., Peterson, B.M., Pogge, R.W., & Pronik, V.I. 2007, ApJ, 668, 708

Shappee, B. J., et al. 2014, ApJ, 788:48

Shen, Y., Richards, G. T., Strauss, M. A., Hall, P. B., Schneider, D. P., Snedden, S., Bizyaev, D., Brewington, H., Malanushenko, V., Malanushenko, E., Oravetz, D., Pan, K., & Simmons, A. 2011, ApJS, 194, 45

Shields, G.A., et al. 2003, ApJ, 583, 124

Smith, J.D., et al. 2004, MNRAS, 350, 140

Starkey, D., Horne, K., Fausnaugh, M.M., et al. 2016, ApJ, 835, 65 (Paper VI)

Storchi-Bergmann, T., Schimoia, J.S., Peterson, B.M., Elvis, M., Denney, K.D., Eracleous, M., & Nemmen, R.S., 2017, ApJ, 835, 236

Strateva, I.V., et al. (2003), AJ, 126, 1720

Treu, T., Woo, J.-H., Malkan, M.A., & Blandford, R.D. 2007, ApJ, 667, 117

Ulrich, M.-H., & Horne, K. 1996, MNRAS, 283, 748

Vestergaard, M. 2002, ApJ, 571, 733

—. 2004, ApJ, 601, 676

Vestergaard, M., Fan, X., Tremonti, C. A., Osmer, P. S., & Richards, G. T. 2008, ApJL, 674, L1
Vestergaard, M., & Osmer, P. S. 2009, ApJ, 699, 800
Vestergaard, M., & Peterson, B.M. 2006, ApJ, 641, 689
Vestergaard, M., Wilkes, B.J., & Barthel, P.D. 2000, ApJ, 302, 56
Wakker, B. P., Lockman, F. J., & Brown, J. M. 2011, ApJ, 728, 159
Wanders, I., et al. 1995, ApJL, 453, 74
—. 1997, ApJS, 113, 69
Welsh, W.F., & Horne, K. 1991, ApJ, 379, 586
Wills, B. J., Netzer, H., & Wills, D. 1985, ApJ, 288, 94
Wills, B.J., & Browne, I.W.A. 1986, ApJ, 302, 56
Xiao, M., et al. 2018, ApJL, 865, L8
Young, S., et al. 2007, Nature, 450, 74
Zu, Y., Kochanek, C.S., & Peterson, B.M. 2011, ApJ, 735, 80